PNAS
www.pnas.org

Supplementary Information for

Membrane perforation by the pore-forming toxin pneumolysin

M. Vögele, R. M. Bhaskara, E. Mulvihill, K. van Pee, Ö. Yildiz, W. Kühlbrandt, D. J. Müller, and G. Hummer*

***Gerhard Hummer**
E-mail: gerhard.hummer@biophys.mpg.de

This PDF file includes:

Supplementary text
Figs. S1 to S22
Tables S1 to S6
Captions for Movies S1 to S4
References for SI reference citations

Other supplementary materials for this manuscript include the following:

Movies S1 to S4

Supporting Information Text

Supplementary Methods

All-atom MD Simulations.

Fitting and refinement of pneumolysin pore structure. The structure of the pneumolysin (PLY) pore was determined by cryo-EM (1). An all-atom model for the WT sequence (Q04IN8) was obtained from 5LY6 after fixing mutations (T172A, G173A, S182A, E260Q, L266A, K268L, and E277Q). The model was first fitted into the cropped EM-density map (EMD-4118) using the rigid-body docking *fit-in-map* tool of Chimera (2). The top fits were ranked and the best-fit protomer orientation (cc=0.87) was then refined using a molecular dynamics flexible fitting (MDFF) procedure (3) (SI Figs. S20B and S21). MDFF runs were set up using VMD (4) and used the CHARMM36m force field (5). Molecular dynamics simulations were carried out using NAMD (6) in vacuum at a temperature of 300 K for 500 ps. Additional forces corresponding to EM density gradients were coupled using an MDFF scaling factor ξ of 0.3. The value of ξ modulates the coupling strength between model and map. The value of 0.3 is balanced and results in weak coupling without overfitting. Restraints preserving secondary structure, chirality, and trans-peptide bond geometry were employed. Initial MDFF runs were followed by short energy minimization runs for 10,000 steps with $\xi = 10$. After refinement, the final protomer structure was compared to the initial model (5LY6) and assessed for the quality of the local fits within the density and structural changes (SI Fig. S21). Finally, protomer coordinates consistent with C_{42} symmetry were generated using SymmDock (7, 8) and fitted into the EM-map using Colores (9), followed by a final round of energy minimization for 10,000 steps (SI Fig. S20).

Simulation setup. We predicted the membrane-adhered part of the PLY monomer X-ray structure (10) using the OPM server (11–13) and placed it into a DOPC membrane with 30 % cholesterol according to the OPM result. The membrane was set up using the CHARMM-GUI membrane builder (14–17) with 150 mM NaCl. For simulations of PLY monomers and oligomers in pore conformation, the respective structures were cut out of the full ring and placed in a DOPC membrane with 30 % cholesterol, again using CHARMM-GUI and 0.15 mol/l NaCl.

Simulation parameters. All atomistic molecular dynamics simulations were performed with the CHARMM36m force field (5, 18, 19) using Gromacs 5.1.4 (20). Water was modeled using the TIP3P model (21). The equations of motion were integrated using the leap-frog algorithm with a 2 fs time step. Temperature was maintained at 310 K using a Nosé-Hoover thermostat (22, 23) (characteristic time $\tau_T = 1.0$ ps). Pressure was maintained at 1 bar with a semi-isotropic Parrinello-Rahman barostat (24) (characteristic time $\tau_p = 5.0$ ps). Bonds to hydrogen atoms were fixed using LINCS (25) and the center-of-mass motion was removed every 100 time-steps. The system was initially energy minimized using a steepest descent algorithm followed by equilibration employing the standard CHARMM-GUI procedure: six rounds of short runs with increasing time steps, using the Berendsen thermostat and barostat (26) along with position restraints on protein atoms.

Contact analysis. For each of the two docking sites (undecapeptide and loop 1) and for each membrane component (cholesterol and DOPC), time series of mutual contacts were calculated using the Gromacs (20) tool `gmx mindist`. Two molecules were defined to be in contact if at least one pair of non-hydrogen atoms was within a distance of 0.6 nm.

Coarse-grained MD simulations of PLY docking.

Simulation setup. We studied the effect of cholesterol on PLY-membrane binding and interactions in simulations of PLY monomer docking to DOPC bilayers containing different concentrations of cholesterol (0%, 15%, 30%, and 50%). 100 replicates of each simulation were performed. The initial configuration contained a bilayer (DOPC + cholesterol) and one solvated PLY molecule between the membrane and its periodic image in a cubic simulation box with an edge length of 20 nm. Semi-isotropic pressure coupling was applied using the Parrinello-Rahman barostat (24) with $\tau_p = 12$ ps. Temperature was kept constant at 310 K using the Bussi-Parrinello thermostat (27). In simulations of protein variants, Trp residues of the undecapeptide and L460 were mutated to alanine (W433A, W433A+W435A+W436A, and L460A) using the WHAT IF server (28) before mapping all-atom models to the coarse-grained MARTINI model.

Criterion for docking. Simulations were analyzed by quantifying protein-bilayer interactions. A PLY monomer was classified as docked to the membrane if at least one contact was present between the undecapeptide (427-437) or Loop 1 (458-461) and the head groups of DOPC (PO4 and NC3 beads) or cholesterol (ROH beads). A bead-distance cutoff of 0.6 nm was used to define contacts. Distance calculations were performed using the Gromacs (20) tool `gmx mindist`.

Coarse-grained MD simulations of PLY rings.

Ring setup. We constructed 42-mer rings by combining given numbers of PLY protomers in prepore and pore conformations, followed by energy minimization. The relaxed PLY rings were adhered to 70×70 nm^2 membrane patches with a 70:30 DOPC:cholesterol ratio, and solvated in water with 0.15 mol/l NaCl in a box of 15 nm height using insane.py (29). Additional simulations were performed using a symmetric two-ring system. In a membrane patch of initially 70×140 nm^2, one ring each was attached to the opposite leaflets followed by equilibration runs. All other properties were chosen identical to the single-ring systems.

Simulation parameters. Complete PLY_{42} rings were simulated using the coarse-grained MARTINI model in single and two-ring setups. We varied the fraction of protomers in pore conformation from 0/42 to 42/42. All systems were first subjected to energy minimization using the steepest descent algorithm, followed by NVT equilibration with fixed protein and lipids for 50,000 steps of 10 fs. Then all restraints were removed, and the simulation was continued for 500,000 steps for NVT equilibration. In the NVT equilibration runs, we used a Berendsen thermostat (26) to keep the temperature at 310 K, using a characteristic time of $\tau_T = 2.0\,\mathrm{ps}$. Then, in an NPT equilibration run of another 500,000 steps, a Berendsen barostat(26) kept the pressure at 1 bar, using a characteristic time of $\tau_p = 4\,\mathrm{ps}$. The production runs in the NPT ensemble were performed with a time step of 20 fs using a Bussi thermostat (27) (310 K, $\tau_T = 1.0\,\mathrm{ps}$) and a semi-isotropic Parrinello-Rahman barostat (24) (1 bar, $\tau_p = 12\,\mathrm{ps}$). The two-ring systems were equilibrated using the $\mathrm{NAP}_z\mathrm{T}$ ensemble for 1 μs, i.e., with pressure coupling in z direction only and constant frame area in the x-y plane to avoid strong membrane deformations after equilibration. Production runs were extended for two-ring systems using the $\mathrm{NAP}_z\mathrm{T}$ ensemble. All other settings were as in the single-ring simulations.

Membrane deflection. Deformations of the membrane patches enclosed by the PLY ring were quantified by measuring the deflection of its midplane. Terminal beads (C4B/C5B) of the enclosed DOPC bilayer lipids were used to approximate a midplane. Their positions were mapped to the coordinate system of the PLY ring. Midplane deflection was then defined as the maximum distance of two such beads along the axis normal to the ring plane. The deflection is maximal for a strongly curved membrane (extreme case: a vesicle) and minimal for a flat membrane.

Elastic model for the membrane patch inside the ring. The balance between bending energy and edge energy dictates the shape of the enclosed membrane. By comparing the elastic energies for flat and vesicular membrane patches of different sizes (SI Fig. S18 B; see details below), we found that the energetically preferred shape is either an open disk or a highly curved vesicle. Using a set of elastic constants typical for cholesterol-rich membranes (30), we found the flat membrane configuration to be favorable up to a pore radius of $R_0 \approx 5$ nm (SI Fig. S18 B). The transition from the initial flat state towards a vesicle still requires crossing a free energy barrier. For very small membrane patches, the barrier can be several hundred $k_\mathrm{B}T$, which would make it practically insurmountable. By contrast, the barrier is lower for larger membrane patches and ultimately vanishes, allowing spontaneous formation of vesicles. At $R_0 = 9.5\,\mathrm{nm}$, the barrier drops below $1\,k_\mathrm{B}T$. This critical size computed from elastic theory roughly matches the observed size distribution of PLY rings observed experimentally by cryo-EM for both prepores and pores (31) (SI Fig. S18 B). A generalization of this model using a spherical-cap approximation for partially inserted pores (see below) shows that also in this case, the preferred membrane shape depends on the pore radius (SI Fig. S19).

Helfrich Hamiltonian. The free energy of an open bilayer membrane is given by (32–34):

$$F = \int (f_c + \lambda)\mathrm{d}A + \gamma \oint_C \mathrm{d}s \qquad [S1]$$

where λ is the membrane surface tension, γ is the line tension on the open edge, and f_c is the local curvature energy per unit area of the bilayer patch. The curved membrane surface is characterized by two principal curvatures, k_1 and k_2, which define the local mean curvature $H = \frac{1}{2}(k_1 + k_2)$ and the Gaussian curvature $K_G = k_1 k_2$. These quantities are used to define the curvature energy per unit area of the elastic membrane,

$$f_c = \frac{\kappa_c}{2}\,(2H + c_0)^2 + \bar{\kappa} K_G\ , \qquad [S2]$$

where c_0 is the spontaneous bilayer curvature, κ_c is the bending modulus, and $\bar{\kappa}$ is the saddle splay modulus.

Geometry. We model the circular lipid patch of radius R_0 with maximal circumference $L_0 = 2\pi R_0$ enclosed by the PLY ring in a simplified way (SI Fig. S22). We assume that a sector with polar angle $2\pi P$ of the PLY ring is in pore conformation. This can be seen as a measure of progress for a hypothetical step-by-step insertion process ($0 \le P \le 1$) involving transitions of individual protomers from the prepore to the pore conformation. As lateral interactions of the inserted β-strands stabilize the pore conformation of PLY, the fraction P quantifies the arc along the circular disc and the angle $\varphi = 2\pi(1 - P)$ denotes the sector of the ring that is still in the prepore conformation (SI Fig. S22). The length of the corresponding fixed edge with lipids is $L_f = \varphi R_0$. The membrane patch close to the hydrophilic inner rim of the ring with edge length recedes, thereby exposing a free edge of length L_e. The edge length of the exposed bilayer disc is variable. It can range from the shortest possible exposed edge length $L_s = 2\,R_0\,\sin(\varphi/2)$ to the entire circular segment $L_p = PL_0$. The total edge length of the resulting membrane patch is $L = L_f + L_e$.

Spherical-cap approximation. We model the shape of the membrane patch inside the PLY ring as a spherical cap with an edge given by the circumference L and radius $a = L/2\pi$. The spherical cap has a fixed surface area $A = \pi(a^2 + h^2)$, with a height h (depth of the cup/bowl) given by $h^2 = A/\pi - a^2$ and a radius r,

$$r = \frac{a^2 + h^2}{2h}\,. \qquad [S3]$$

The spherical cap has constant curvature, i.e., $k_1 = k_2 = 1/r$ along its entire surface and therefore a constant bending energy per unit surface area f_c, which simplifies the Helfrich Hamiltonian to an area term and an open edge term,

$$F = A\,(f_c + \lambda) + \gamma\,L_e\ . \qquad [S4]$$

The local curvature along the lipid patch is variable in real systems. The curvature is small closer to the ring segments in prepore conformation, i.e., along L_f, but higher at the free exposed edges. These effects are partially cancelled in the integral, improving our approximation. Because the free energy would be variationally minimized over all shapes, given the constraints, the free energy for the spherical cap is larger than the minimum free energy. In the absence of spontaneous curvature, i.e., $c_0 = 0$ for flat PC-rich membranes, and excluding Gaussian curvature effects, the bending energy effectively is obtained from the mean curvature k of the spherical cap (30),

$$f_c = 2\kappa_c k^2 \ . \qquad \text{[S5]}$$

Constant area. Under confinement, lipids cannot flow in and out of the PLY ring, keeping the area of the membrane patch constant, $A = A_0 = \pi R_0^2$. The term $A\lambda$ results in the addition of a constant and can therefore be neglected. This leads to further simplification of the Helfrich free energy, which now only depends on the constant curvature k of the spherical cap and the length L_e of the exposed free edge

$$F = 2\kappa_c A k^2 + \gamma L_e. \qquad \text{[S6]}$$

The height of the spherical cap, representing the magnitude of the deformation of the bilayer patch is given by $h^2 = R_0^2 - a^2$ and by Eq. **S3** with (constant) curvature

$$k = \frac{1}{r} = \frac{2}{R_0}\sqrt{1 - \left(\frac{a}{R_0}\right)^2}. \qquad \text{[S7]}$$

Supplementary Results

Elastic membrane model for partial insertion. In the following, we use the elastic membrane model to predict the behavior and shape changes of the enclosed lipid patches in case of a slow or an incomplete transition. Looking only at a free, completely excised membrane patch enclosed by the PLY ring, we assumed that pore formation is instantaneous. However, the exact mechanism of insertion of the β-sheets is not clear and several scenarios are possible.

Here we assume the mechanism of pore formation to proceed by a continuous prepore-to-pore transition to begin at one point along the ring and propagate along both directions along the ring. Our elastic model accounts for the resulting increase in the edge length L_e of the free exposed edge as more protomers transition into pore conformation. The value of L_e characterizes the enclosed membrane shapes. Large values of L_e are associated with flat membrane shapes whereas smaller values L_e are associated with a membrane that is highly curved in order to decrease the length of its free edge. For a closed vesicle with no free edge, $L_e = 0$.

The minimum free energy shape for the enclosed bilayer patch is either the flat circular disk (as in a fully formed prepore ring) or a curved, cup-shaped structure (Fig. S19). The latter is analogous to the closed vesicle structure, a limiting case that is formed upon complete insertion of all protomers during the final steps of pore formation. Therefore, the preferred configuration of the enclosed membrane can vary from flat to curved membrane shapes during intermediate stages along pore formation.

The barrier for a transition from a flat membrane to a curved bowl shape is large. At the beginning of the process, the free energies of both states are very similar and the shapes could interchange easily, as the induced curvature is relatively small. As pore formation proceeds, the barrier between the two states increases with a finite difference between the two minima. However, as the energy of the bowl shape drops further, the maximal free energy between the states remains the same. The height of the barrier is therefore constant within the range of $F_{\text{bowl}} < F_{\text{vesicle}}$, indicating no alternate route to transform into a curved configuration from a flat disc.

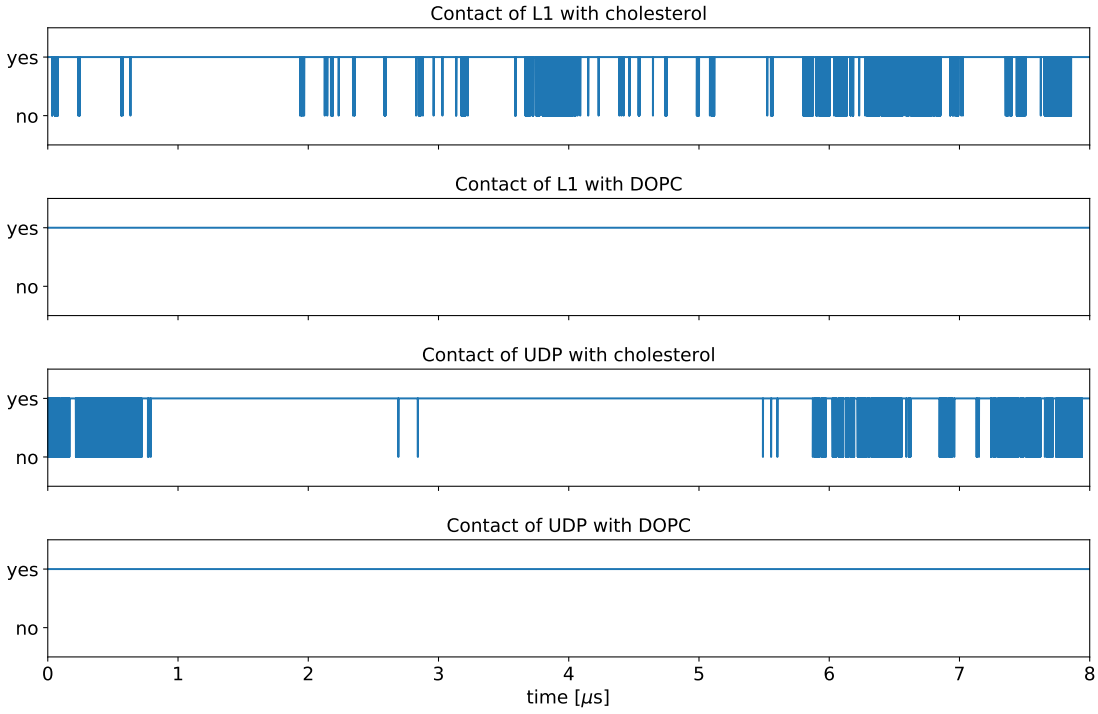

Fig. S1. Time series of contacts between PLY and membrane components. Contacts of L1 and undecapeptide (UDP) residues in PLY with cholesterol and DOPC lipids in the membrane were defined using a 0.6-nm distance cutoff for non-hydrogen atoms. During the entire 8-μs long all-atom simulation of a membrane-adhered PLY monomer, both the UDP and L1 docking sites were always in contact with at least one DOPC molecule and most of the time also with a cholesterol molecule.

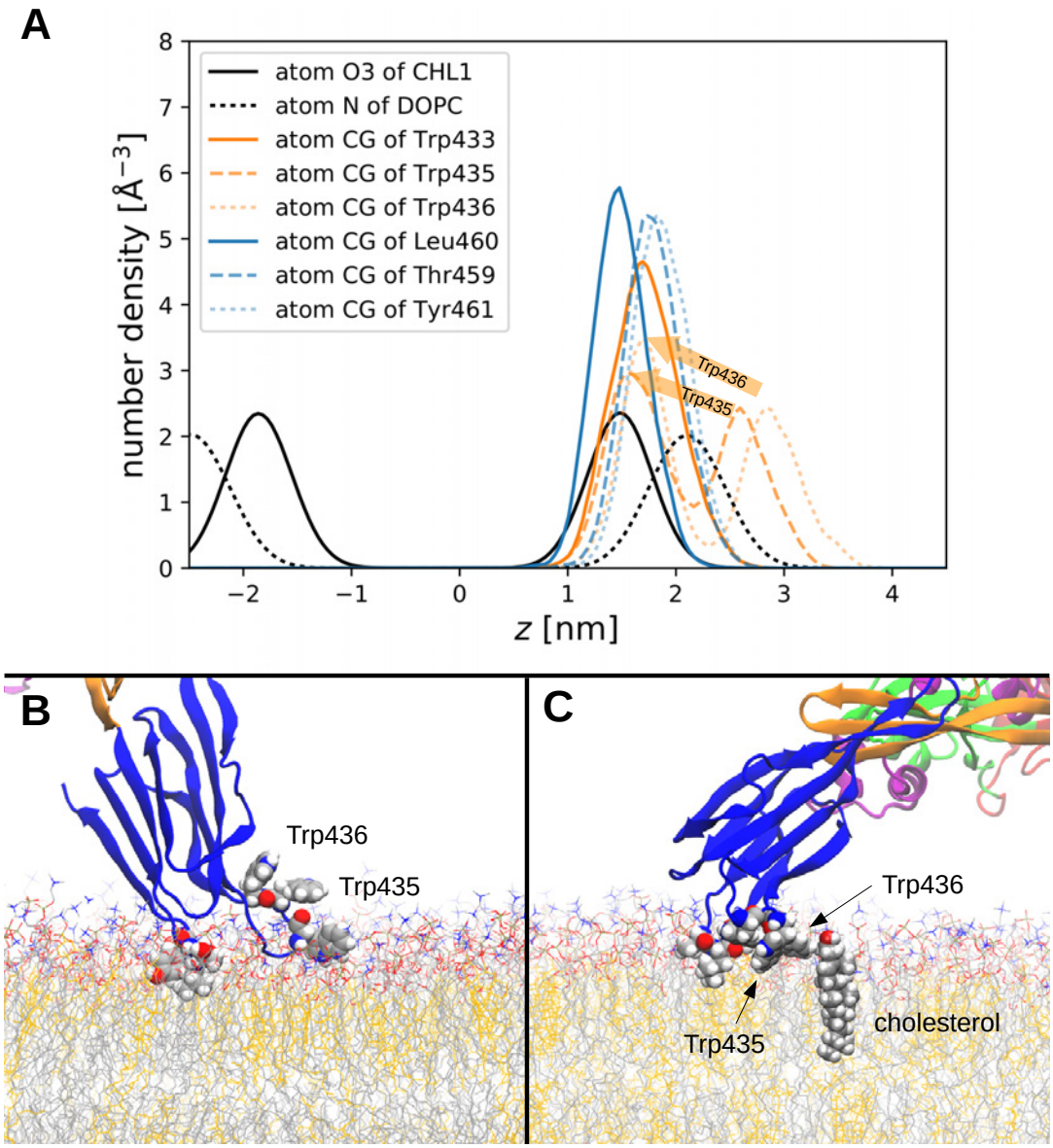

Fig. S2. Membrane-protein interactions in the all-atom simulation of a membrane-adhered PLY monomer. (A) Relative position of membrane-interacting residues (Trp, Leu, Thr and Tyr colored red, orange and blue) with respect to the bilayer-z (black; bilayer midplane at $z = 0$) for prepore PLY-membrane complex. Number density (normalized by the total number of atoms in the system) for interacting residues of D4 compared to the head groups of the membrane lipids (DOPC and cholesterol) shows that the docked complex is stabilized by cholesterol interactions on the upper leaflet (1-2 nm). (B) Configuration before the rearrangement of the two tryptophan residues in the undecapeptide. (C) Configuration after the rearrangement. Trp435 and Trp436 are now attached to the membrane. The image shows an illustrative interaction of Trp436 with cholesterol.

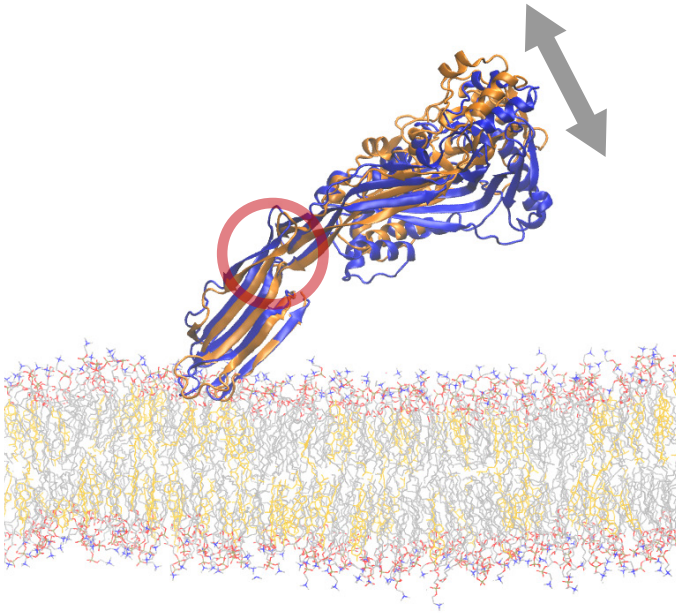

Fig. S3. Hinge motion of the docked monomer. Shown are the equilibrated starting structure (orange) and the final structure (blue; after 8 μs) of the all-atom MD run of membrane-adhered PLY. The hinge is marked with a red circle and the motion is indicated by gray double-arrows.

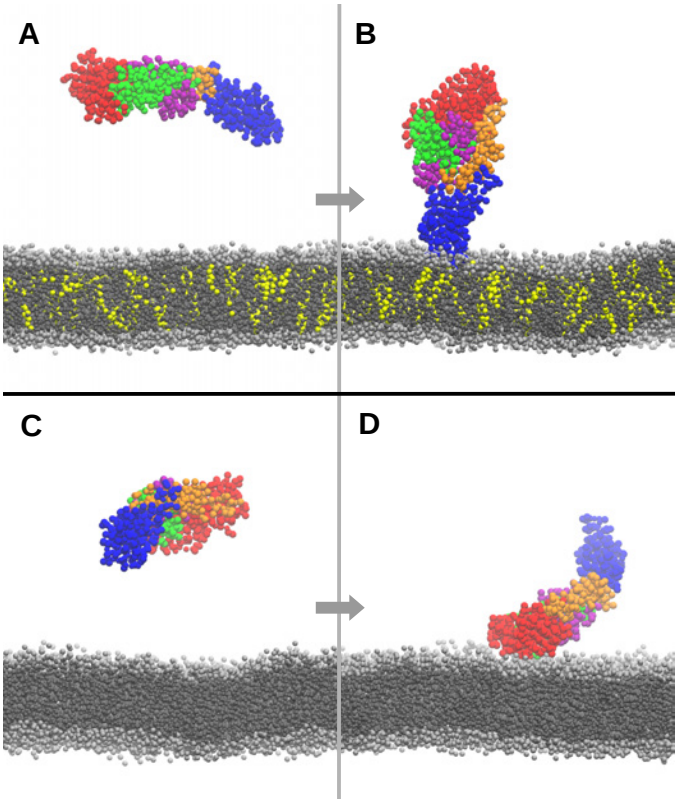

Fig. S4. Role of cholesterol in docking of PLY-monomers to membranes. Selected snapshots from a coarse-grained molecular dynamics simulation, showing intermediates along a membrane-docking event in the presence (A, B) and absence of cholesterol (C, D). (A) Initial configuration showing the PLY monomer (colored) and the DOPC membrane (gray) with 30% cholesterol (yellow). (B) Docked conformation of PLY monomer showing the interaction of D4 (undecapeptide and L1) with the upper leaflet. (C) Starting configuration of a simulation in the absence of cholesterol. (D) The PLY monomer does not dock but loosely interacts with the membrane via D1. No undecapeptide and L1 interactions were observed with the membrane, indicating the importance of cholesterol.

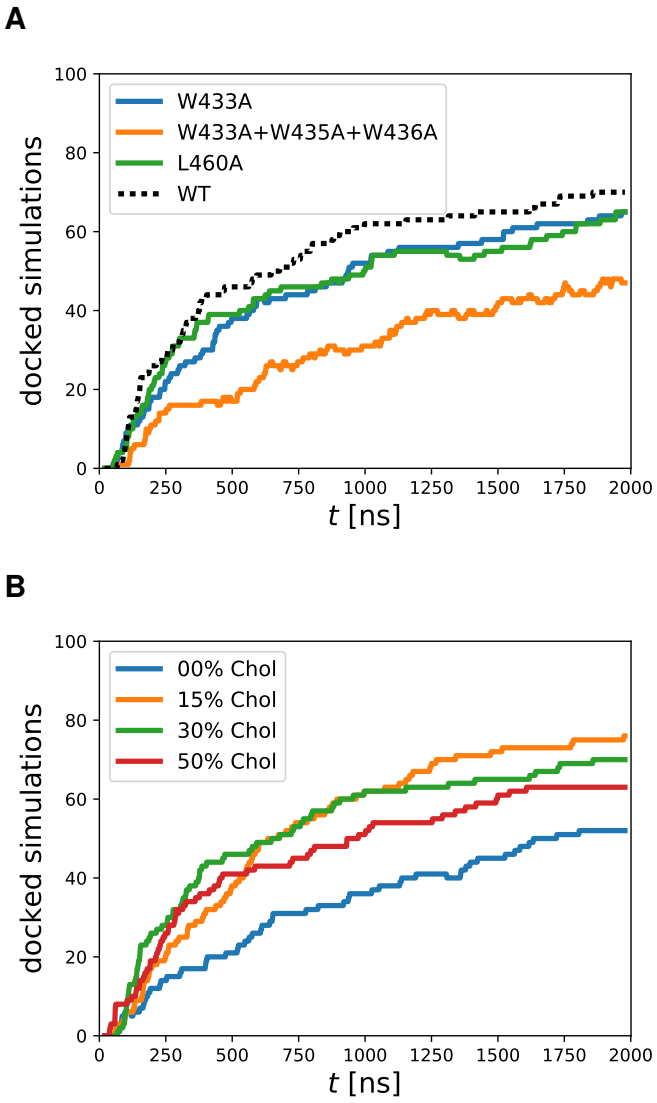

Fig. S5. PLY-membrane docking. Time dependence of the number of PLY monomers docked to a cholesterol-rich membrane out of 100 coarse-grained simulations. Each simulation contained one monomer that was in solution at the start. (A) Comparison of WT PLY with mutations in L1 residues of D4 (at 30% cholesterol) results in smaller number of total docking events and longer waiting times in comparison to WT PLY. (B) Increasing cholesterol concentration in DOPC bilayers increases the overall number of docked PLY monomers.

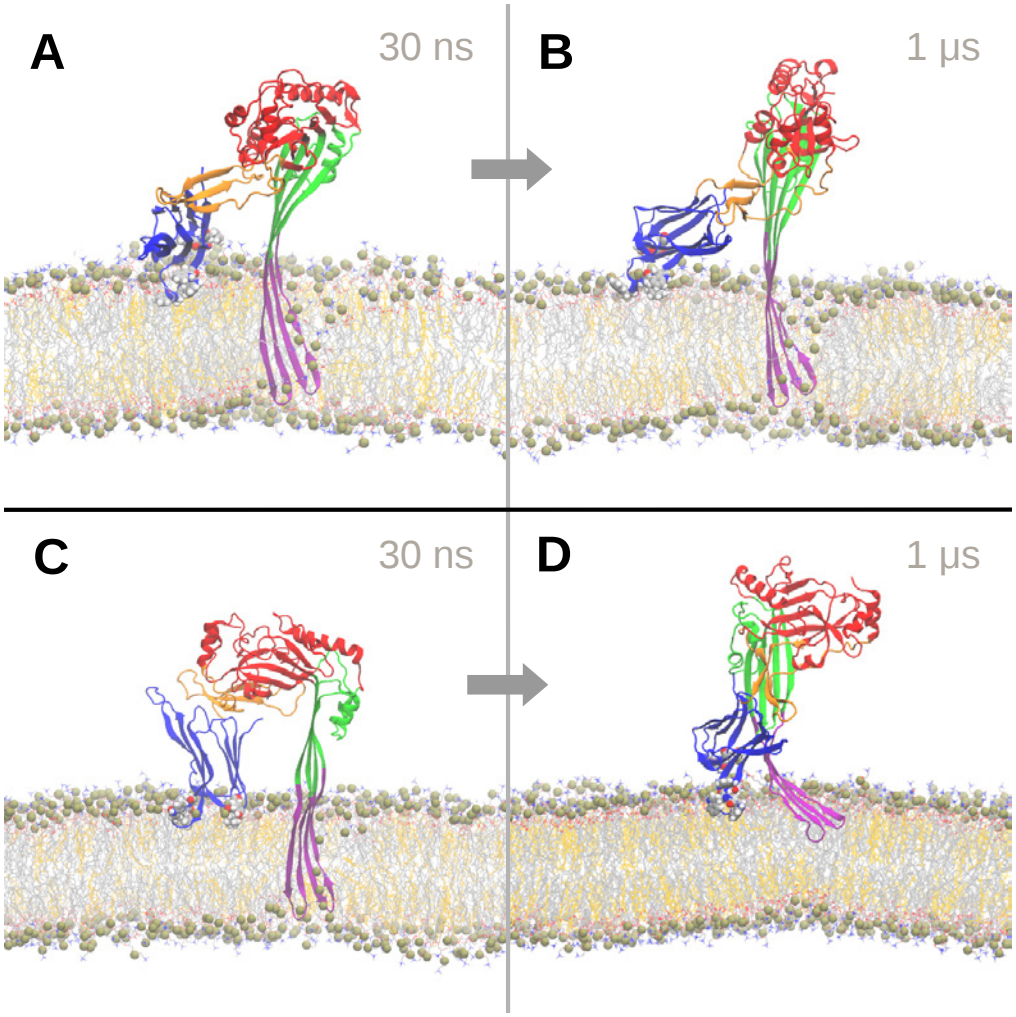

Fig. S6. Structure of PLY monomers embedded in a bilayer. Two atomistic simulations of PLY monomers initiated from the membrane-embedded pore conformation were performed. In the first simulation (A, B), the transmembrane β-strands remain inserted, pulling water and head groups inside the membrane, whereas the other domains of PLY are heavily distorted. In the second simulation (C, D), the transmembrane β-strands are pushed out of the bilayer, indicating that the transmembrane conformation of a PLY monomer is unstable.

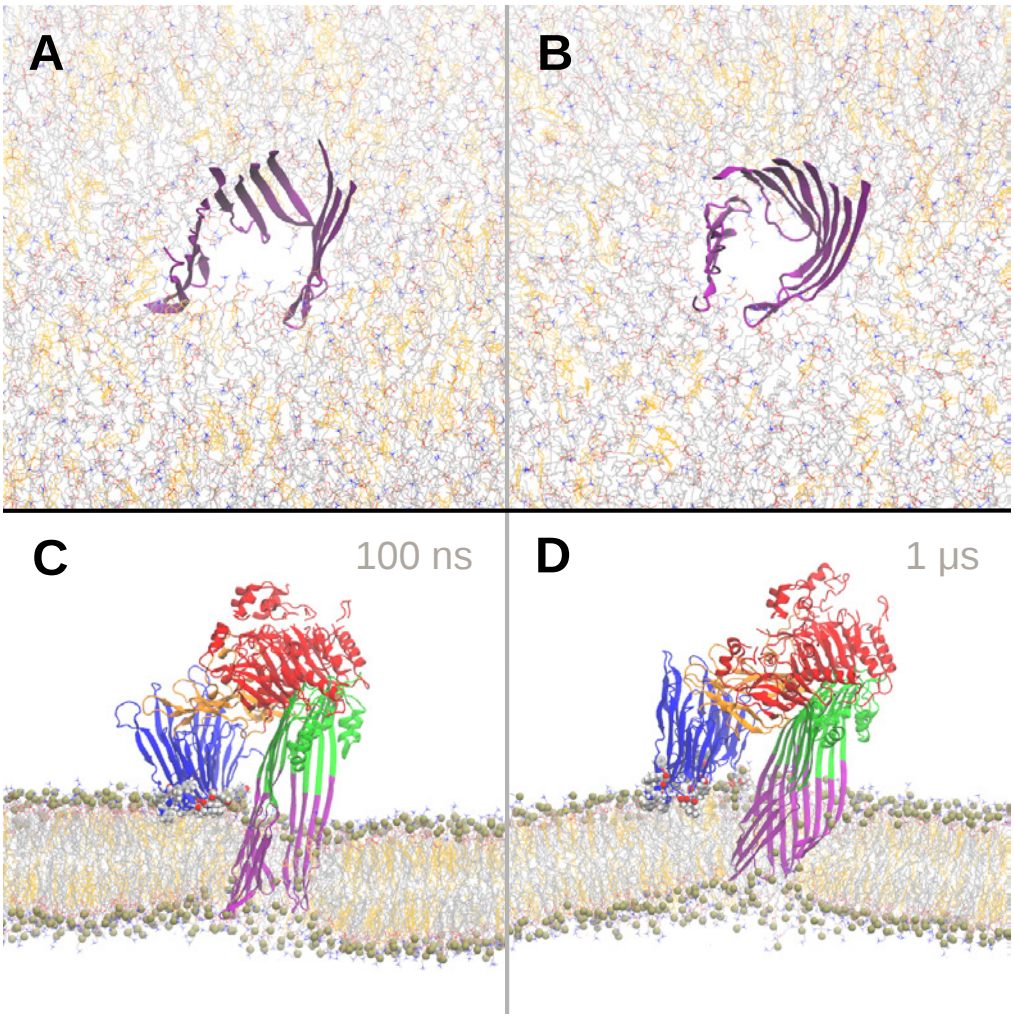

Fig. S7. Structure of a PLY trimer with inserted β-sheets embedded in bilayer. Selected snapshots showing top (A, B) and side views (C, D) of a PLY trimer from atomistic simulations. The transmembrane β-sheet (purple) formed by the three protomers adopt an arc-shape whose inner face is hydrophilic. The arc was heavily distorted already during the first 100 ns. After $1\ \mu$s, an incomplete and contorted barrel-like shape was formed by the reorganized β-sheet.

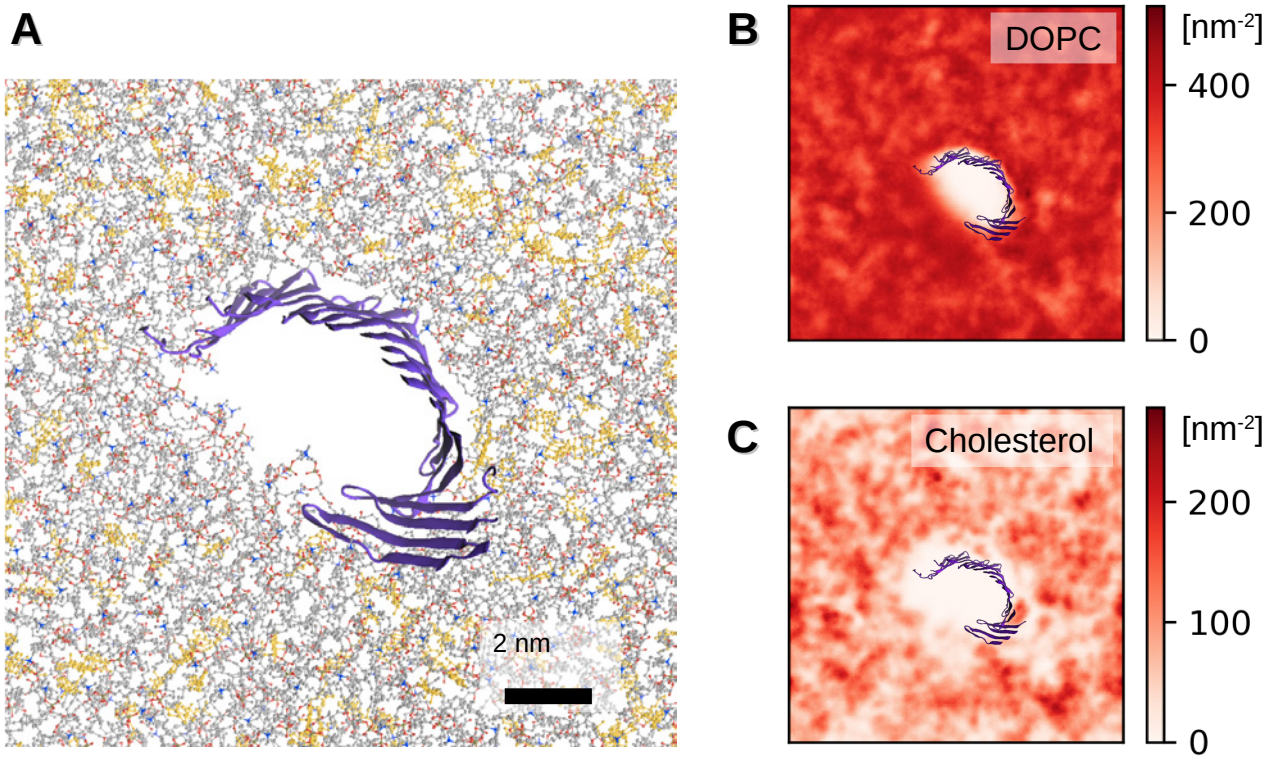

Fig. S8. Lipid fingerprint of the PLY pentamer simulation. (A) Top view on the pentamer simulation after 1.1 μs with only the inserted β-sheets shown. (A) Area density of DOPC atoms and (B) area density of cholesterol atoms, both averaged over the last 200 ns of the simulation.

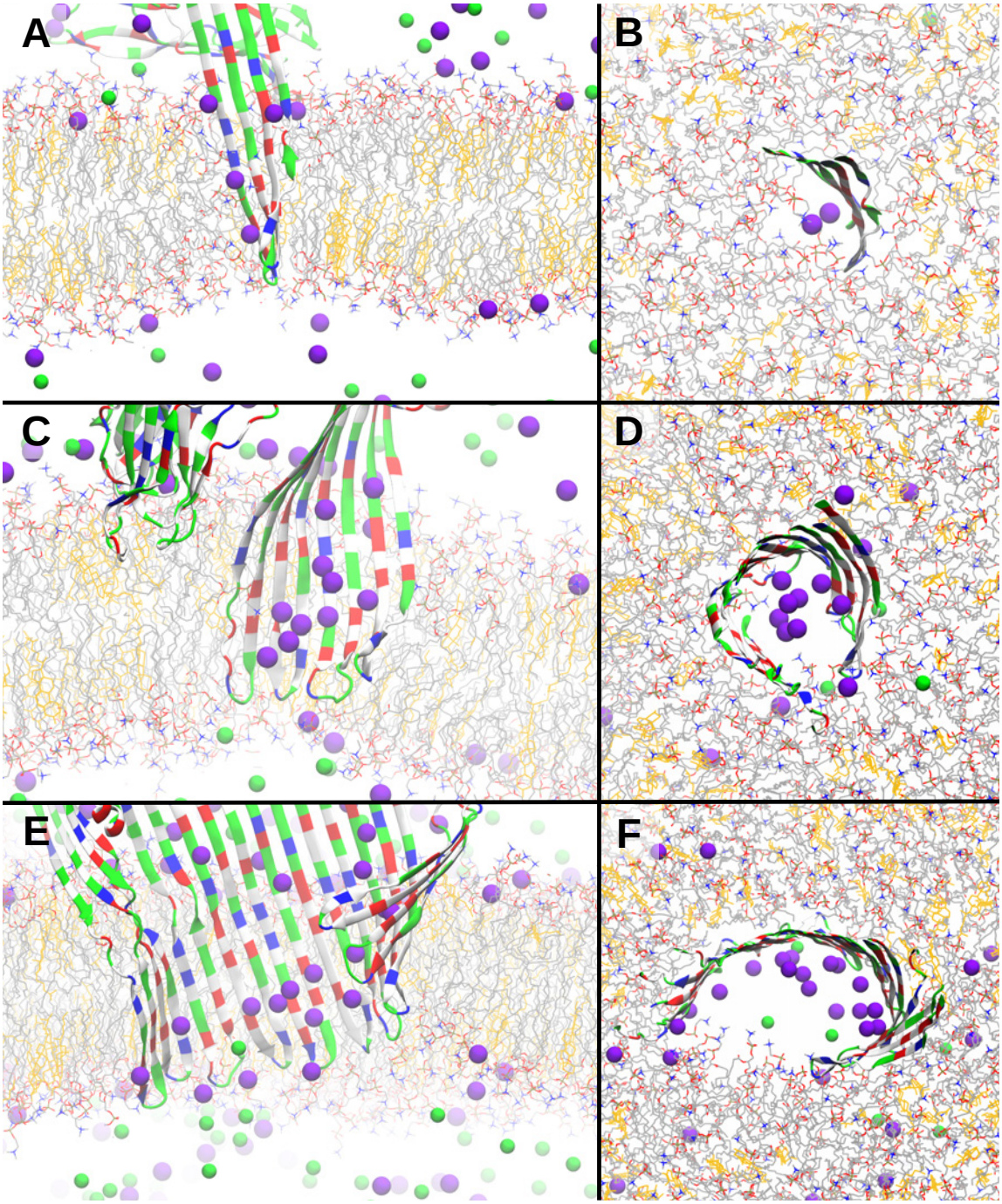

Fig. S9. Behavior of ions around inserted β-sheets. Selected snapshots from the atomistic simulations of the monomer (A, B), the trimer (C, D), and the pentamer (E, F). Side views are shown on the left side, with corresponding top views on the right. The protein is shown in cartoon style with non-polar residues in white, basic residues in blue, acidic residues in red, and polar residues in green. Sodium ions are shown as purple spheres and chloride ions as green spheres.

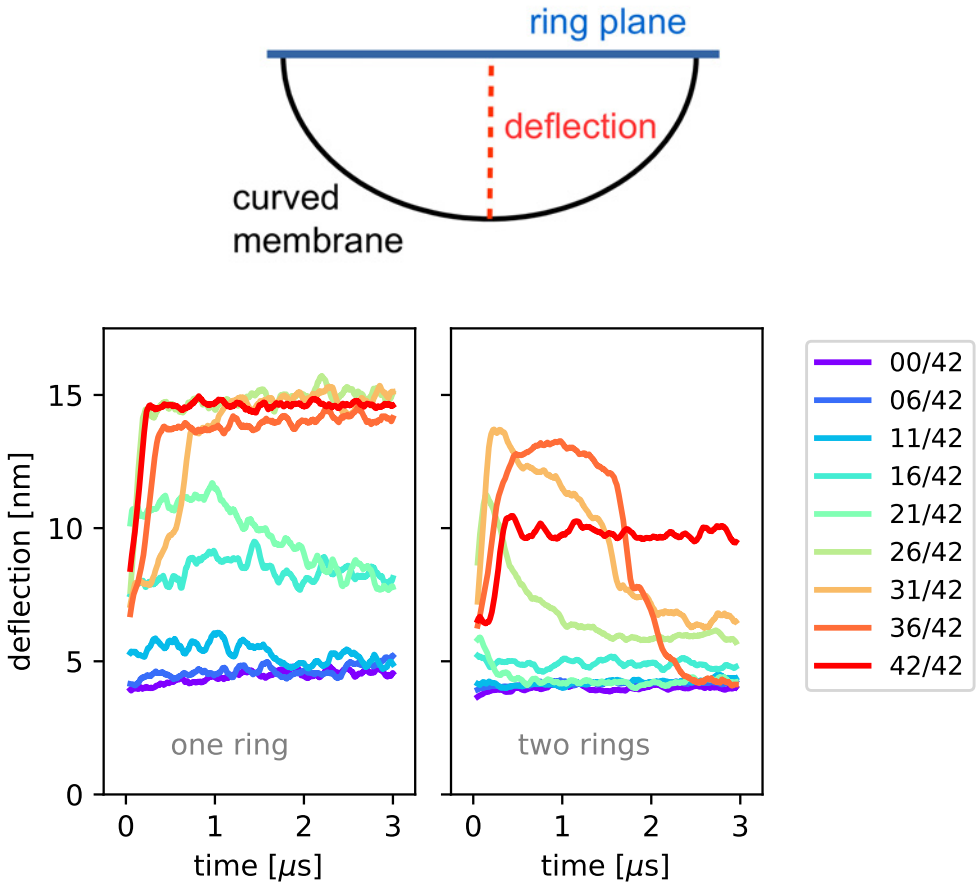

Fig. S10. Shape deformation of the membrane patch within the PLY ring. The deformation of the membrane shape (top; black line) of the enclosed lipid-patch is quantified by measuring the maximum vertical deflection (top; red dashed) from the ring plane. Changes in membrane shape are quantified by measuring the deflection over time for single-ring simulations (left) and two inverted-ring simulations (right) for various intermediate states along the ring insertion pathway. For example, 21/42 indicates simulations of rings with 21 protomers in pore conformation out of a total of 42 protomers. For single-ring systems, the deflection at intermediate stages is appreciable because restricted lipid-flow leads to the formation of curved membrane patches. In the inverted two-ring system, the membrane shape deformations are only prominent with more than 50% of the protomers in pore-conformation. The time-dependence of the deflection indicates that lipid flow out of the ring dissipates deformed membrane shapes.

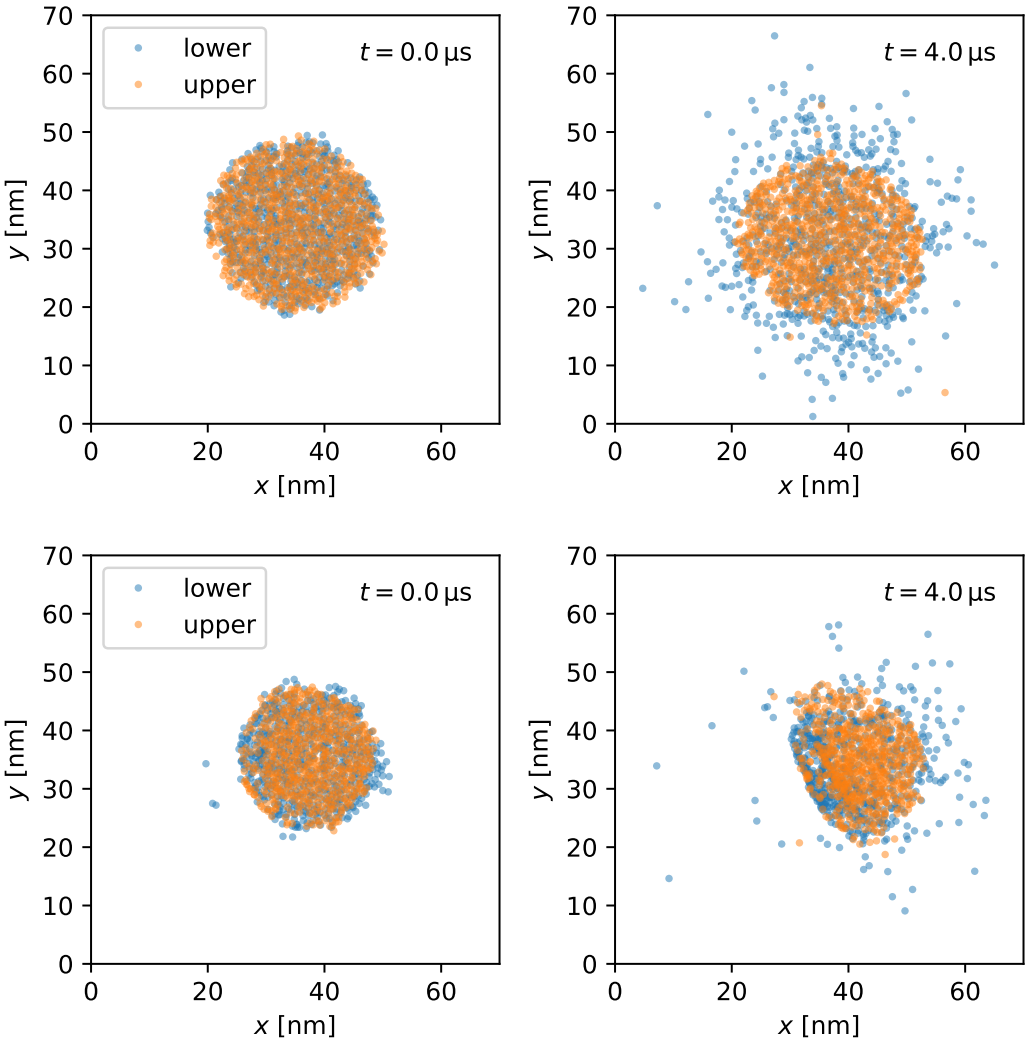

Fig. S11. Lipid diffusion and escape from PLY rings in MD simulations with single rings. We plot the positions of the PO4 beads of the DOPC lipid plug in the membrane plane for upper (orange) and lower (blue) leaflets at the beginning of the simulation and at 4 μs. (Top) PLY ring with all protomers in prepore conformation. Lipid escape into the bulk is largely blocked in the upper leaflet, with a few lipids passing underneath the PLY ring. (Bottom) Half the ring in pore conformation. Lipids from the upper leaflet can cross the open edge of the detached plug and escape via the lower leaflet through the prepore gap. See setup 1 in schematic SI Fig. S9 for the direction of lipid flow.

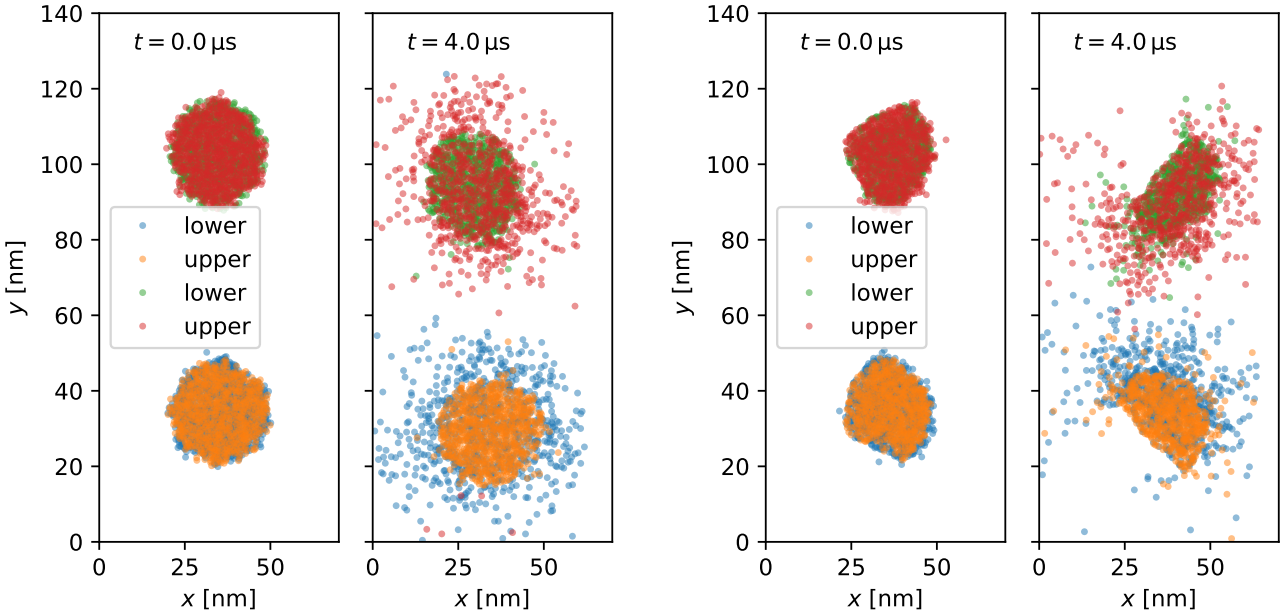

Fig. S12. Lipid diffusion and escape from PLY rings in MD simulations with two inverted rings. We plot the positions of the PO4 beads of both DOPC lipid plugs in the membrane plane for upper (orange and red) and lower (blue and green) leaflets at the beginning of the simulation and at 4 μs. (Left) PLY ring with all protomers in prepore conformation. Lipid escape into the bulk is largely blocked in the upper leaflet, with a few lipids passing underneath the PLY rings. (Right) Half the ring in pore conformation. Lipids from the upper leaflet can cross the open edge of the detached plug and escape via the lower leaflet through the prepore gap. See setup 2 in schematic SI Fig. S9 for direction of lipid flow.

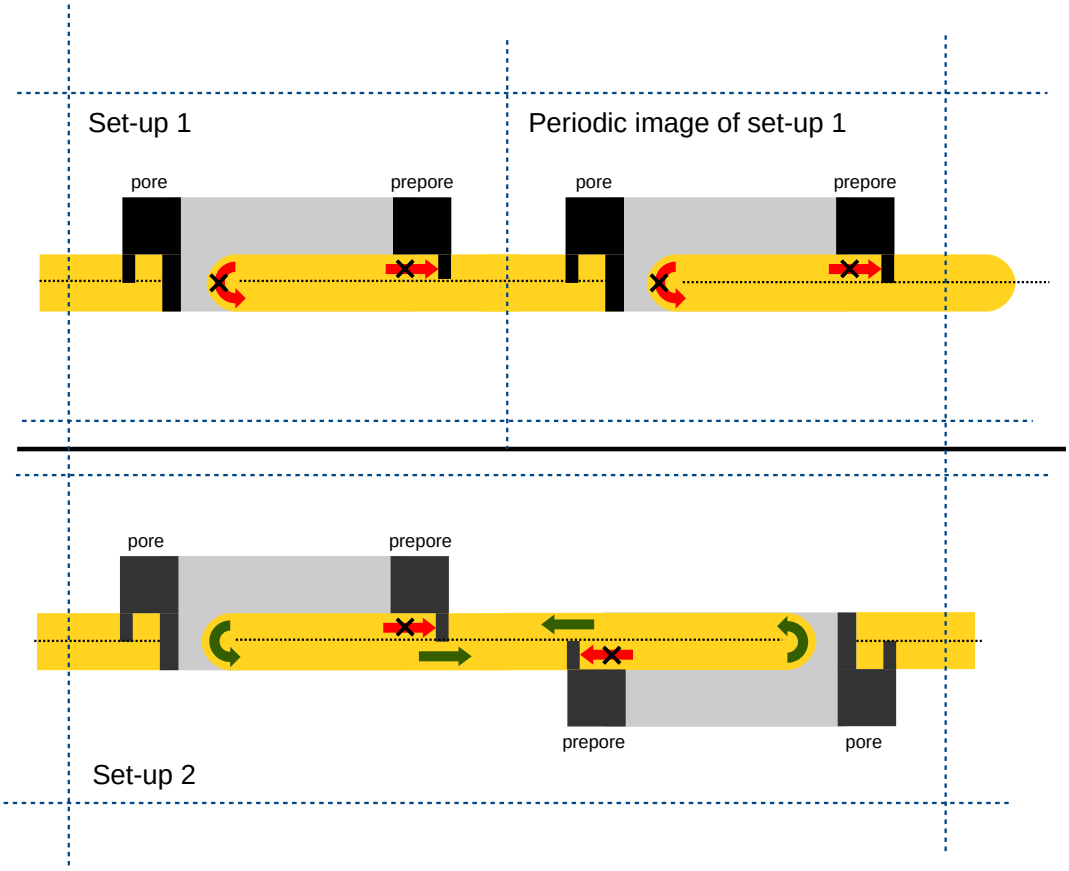

Fig. S13. Lipid efflux from PLY rings in molecular dynamics simulations under periodic boundary conditions. Possible scenarios showing pathways of lipid flow and exchange in simulations under periodic boundary conditions for a single-ring system (top) and a system with two inverted rings (bottom). Lipid flow in the upper leaflet is obstructed because their head groups are trapped by D4 of the docked PLY ring. In the single-ring system, lipid flow across the open edge of the lipid plug inside the partially inserted ring would lead to a number asymmetry between the leaflets, and is thus suppressed (top; setup 1). In the system with two rings on opposite sides of the membrane, the asymmetry caused by lipid flow across the edge in pore 1 is exactly compensated by lipid flow across the edge in the oppositely oriented pore 2 within the periodic box (bottom; setup 2). Note that setup 2 is not physiological, but used here to mimic lipid escape into a large membrane system where the resulting number asymmetry would not cause significant back-pressure.

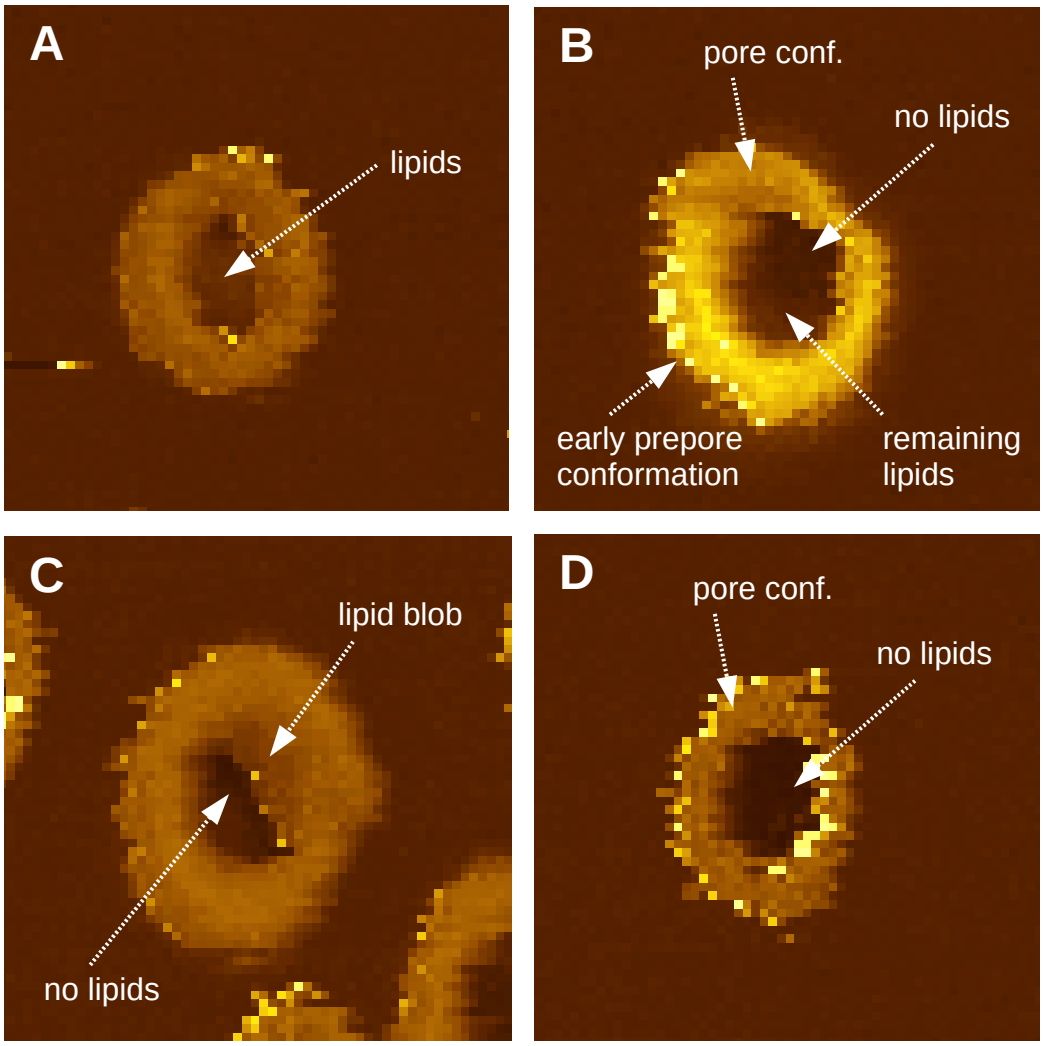

Fig. S14. Selected examples of PLY rings imaged by high-resolution AFM (35). (A) Late prepore with an intact membrane inside. (B) Partially inserted PLY ring with about half of the protomers in early prepore conformation. Lipids are visible only close to the non-inserted region of the ring. (C) PLY ring presumably with a lipid blob inside. (D) Fully inserted ring with completely formed pore. The pores displayed in A, B, C, and D are numbers 3, 19, 46, and 41 in SI Fig. S15, respectively.

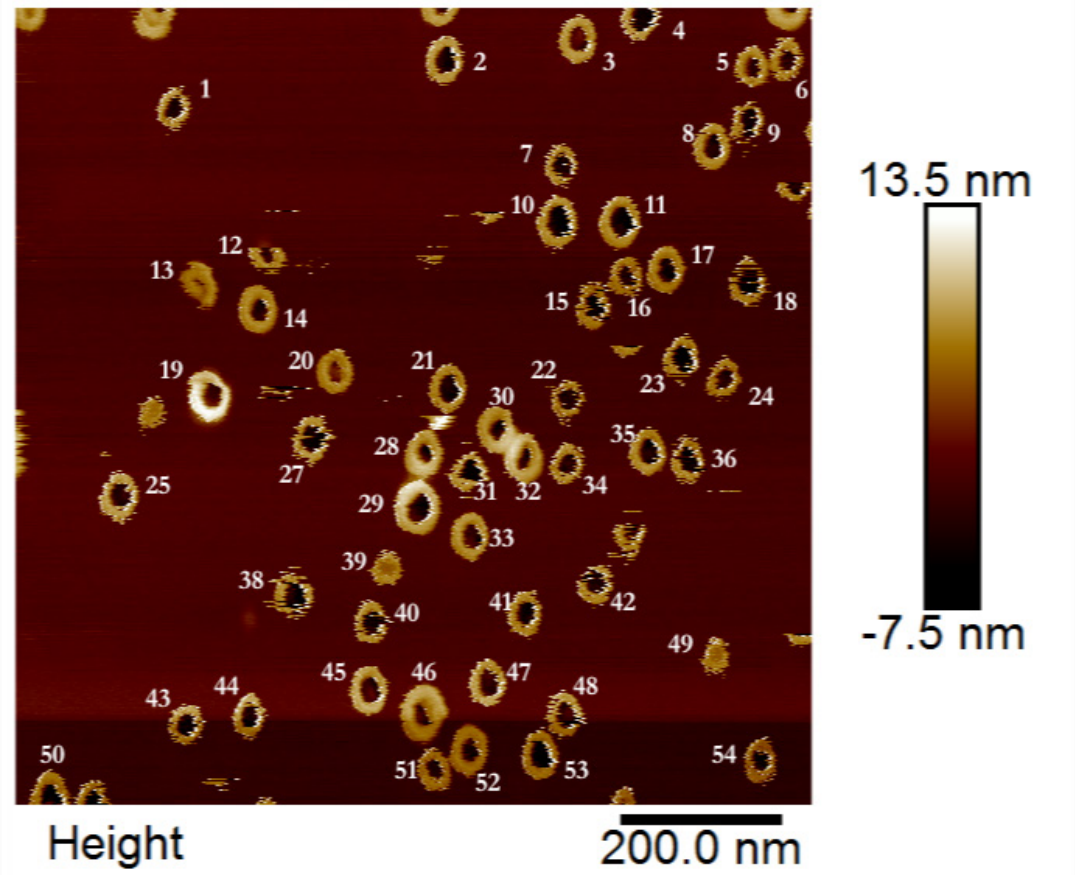

Fig. S15. PLY rings imaged using high-resolution AFM experiments (35). Several rings (numbered) imaged were subjected to analysis and computation of height profiles (see SI Fig. S16).

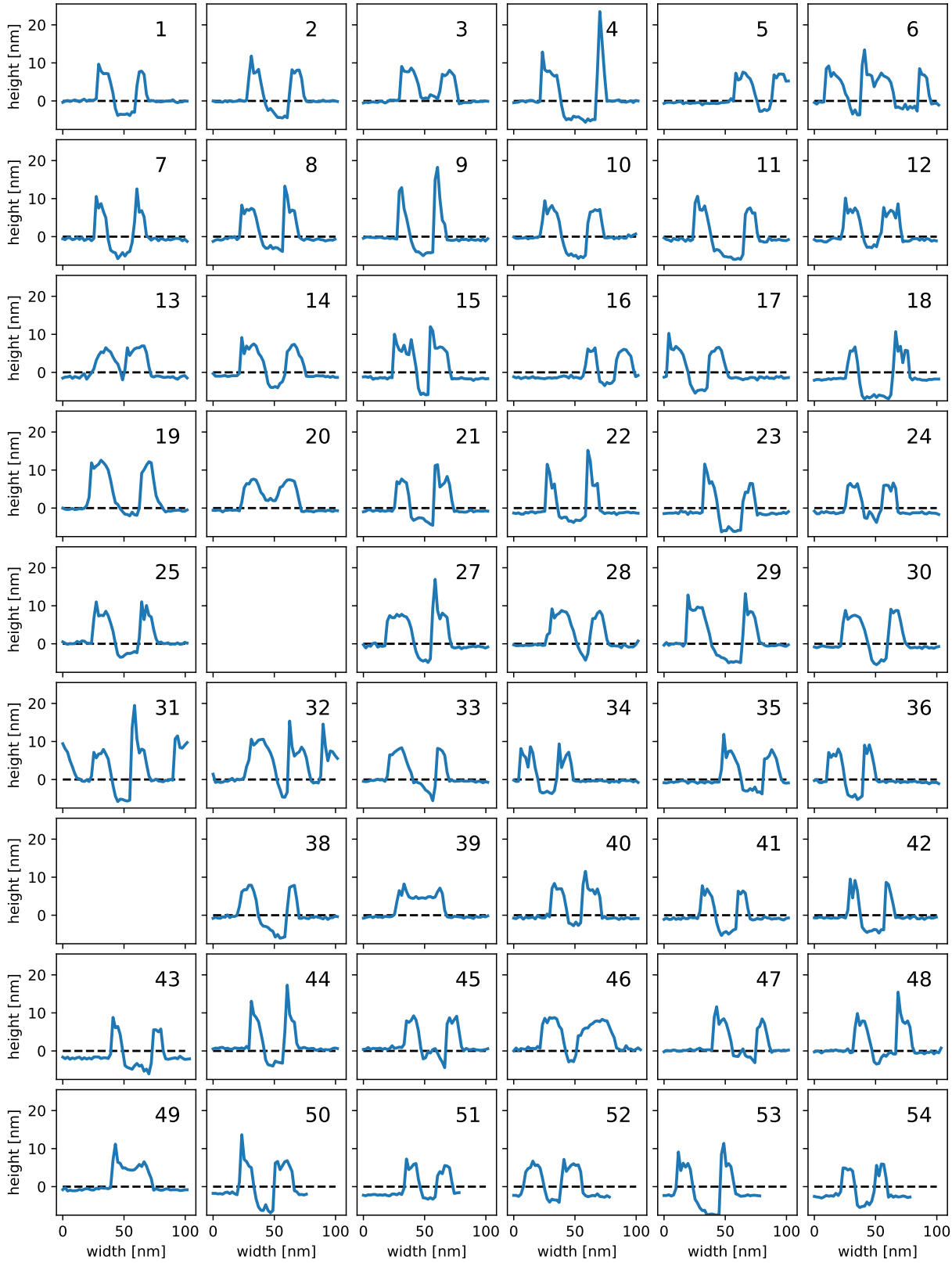

Fig. S16. Height profiles of PLY rings imaged using high-resolution AFM experiments (35). The profiles for individual PLY rings (numbered as in SI Fig. S15) were scanned laterally (horizontal direction passing through the center of the ring). The presence of two peaks with a single trough in between corresponds to PLY segments in either prepore (with heights $\sim$ 11-15 nm) or pore conformation (with heights $\sim$7-10 nm). The flat profile of the trough in between indicates intact plugs (with heights close to baseline $\sim$ 0) and open pores (with heights $\sim$ -4 nm), respectively. A change in profile in between the peaks with large deviations from flatness (with heights $> |4|$ nm) indicates bent lipid patches (see SI Fig. S17).

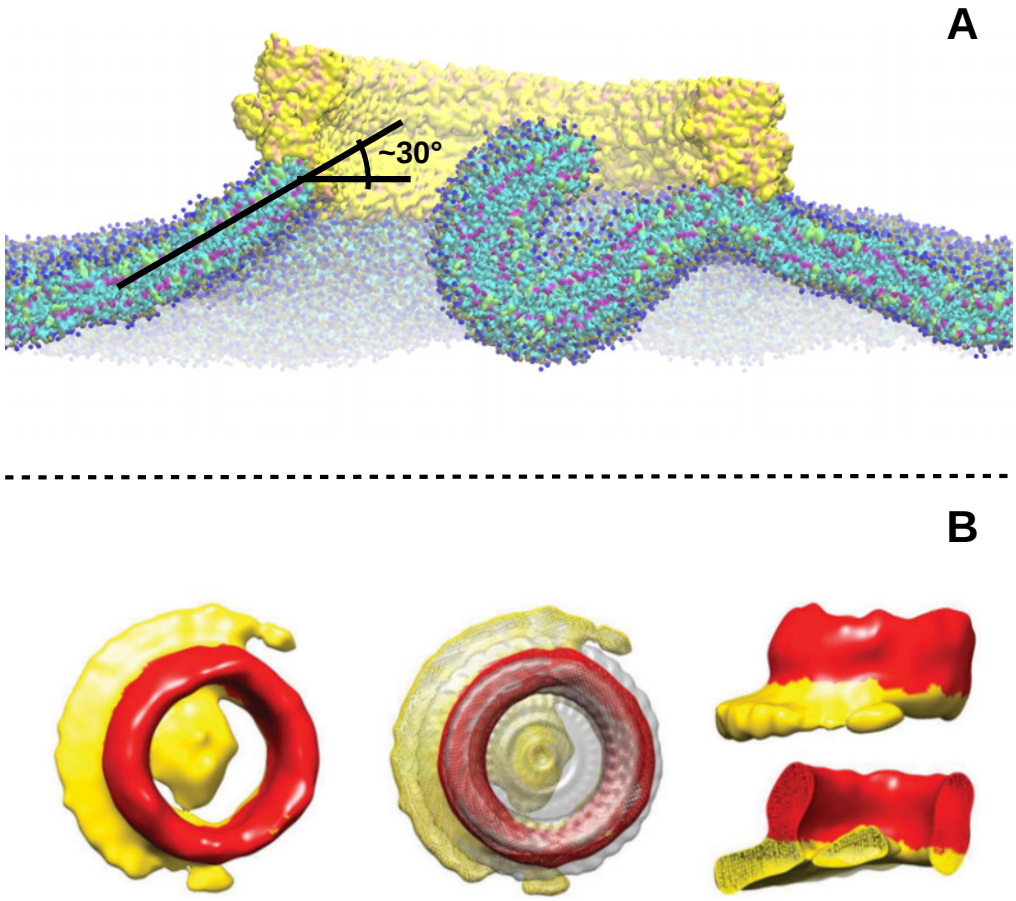

Fig. S17. Comparison of lipids inside the ring. (A) Cross-section of a coarse-grained simulation of a partial 42-mer PLY pore with 26/42 protomers inserted. The angle of the membrane mound around the pore agrees well with cryo-EM maps (31). (B) Sub-tomogram class average of intermediate PLY rings with partial pores observed *in situ* on liposomal membrane, adapted with permission from ref. 36, which is licensed under CC BY 3.0.

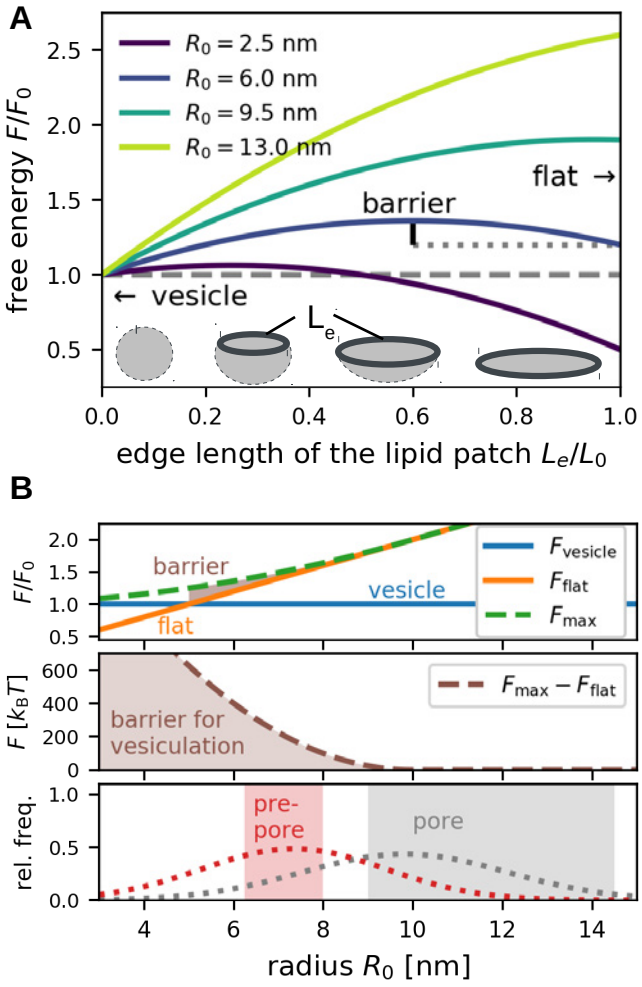

Fig. S18. Elastic energy of detached bilayer patch enclosed by PLY rings in units of $F_0 = 8\pi\kappa_c$, the bending energy of a vesicle. (A) Helfrich elastic energy, F, associated with shape changes of differently sized enclosed membrane patches from flat-bilayer disks $L_e/L_o = 1$ to closed vesicles $L_e = 0$ using a spherical cap approximation. The relative stability of the closed vesicle and flat membrane disk depends on the inner-ring radius R_0 of the enclosed membrane patch. The barrier separating the two states is given by the maximum energy along the transition, $F_{\max}$. (B) The energy barrier for bending the membrane and adopting a curved-vesicle structure decreases with increasing ring radius, R_0. Red and grey shaded regions mark the size-range of PLY rings in prepore and pore conformations from cryo-EM (31) and the dotted curves give the corresponding distribution from AFM experiments (35). Results are shown for bending modulus $\kappa_c = 100\,k_BT$, which is typical for a sterol-rich membrane (30, 37), and a line tension $\gamma = 80\,k_BT/\mathrm{nm}$ (38).

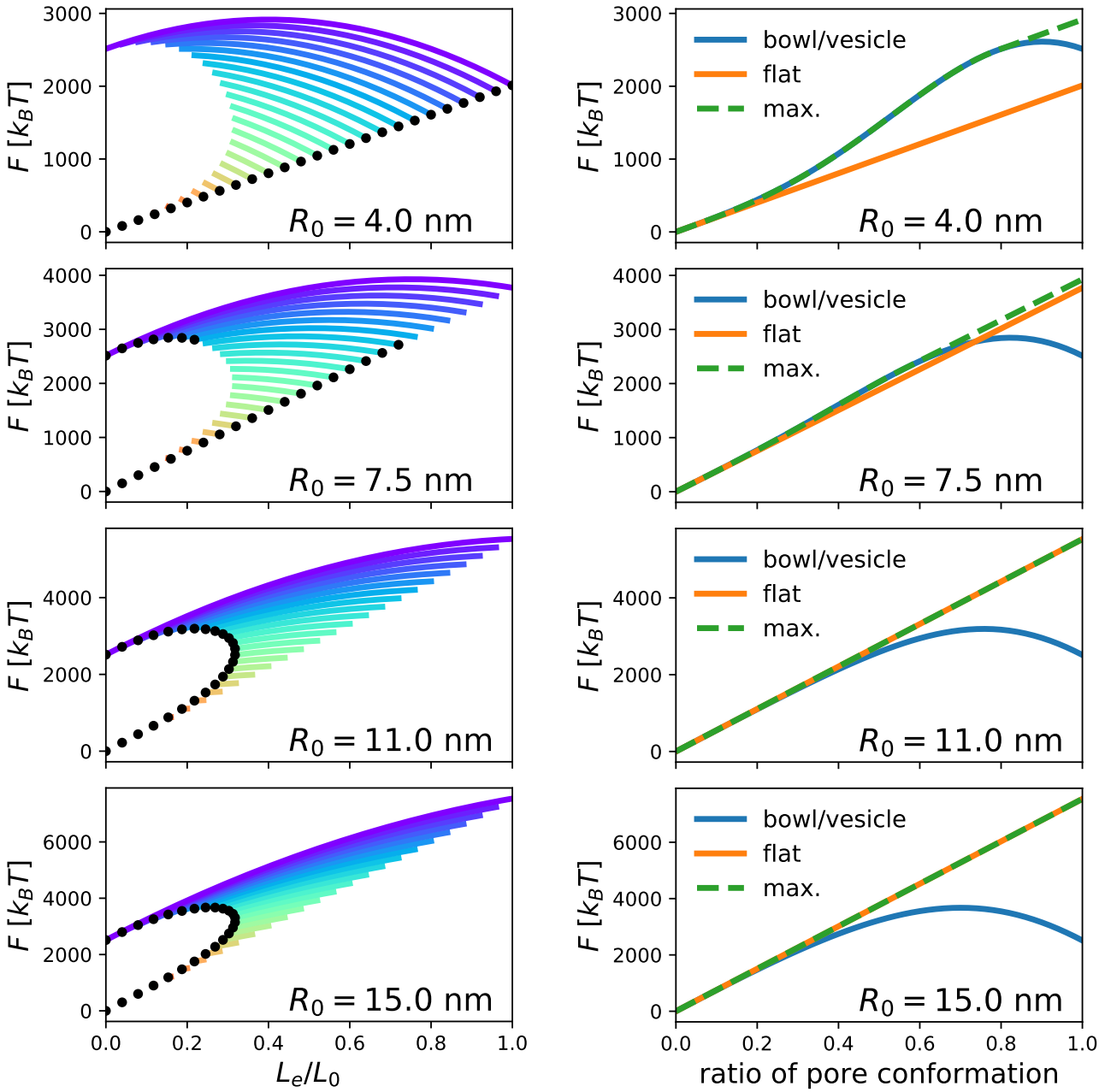

Fig. S19. Free energy of membrane patches in partially inserted PLY rings. Left: Helfrich free energy F computed by varying L_e for a given stage of ring insertion given by L_e/L_0 (individual lines). Early and late intermediate stages along the pore-insertion process are colored from red to blue. Free energies for four different ring sizes $R_0 = (4.0, 7.511.0, 15.0)$ are computed. Lowest free energy values along each line for given L_e/L_0 are marked (black dots). Right: Free energy for the two limiting cases, i.e., a flat membrane disc (orange; scales linearly with exposed edge length L_e) and a bowl shape (blue; Helfrich bending energy given by curvature of the spherical cap) as a function of progress along pore conformation is plotted for the four different pore sizes. The maximum free energy of the intermediate between the two states (green) is also shown as a function of progress along the pore formation pathway. Results are shown for a bending modulus $\kappa_c = 100\,k_\mathrm{B}T$, which is typical for a sterol-rich membrane (30, 37), and a line tension $\gamma = 80\,k_\mathrm{B}T/\mathrm{nm}$ (38).

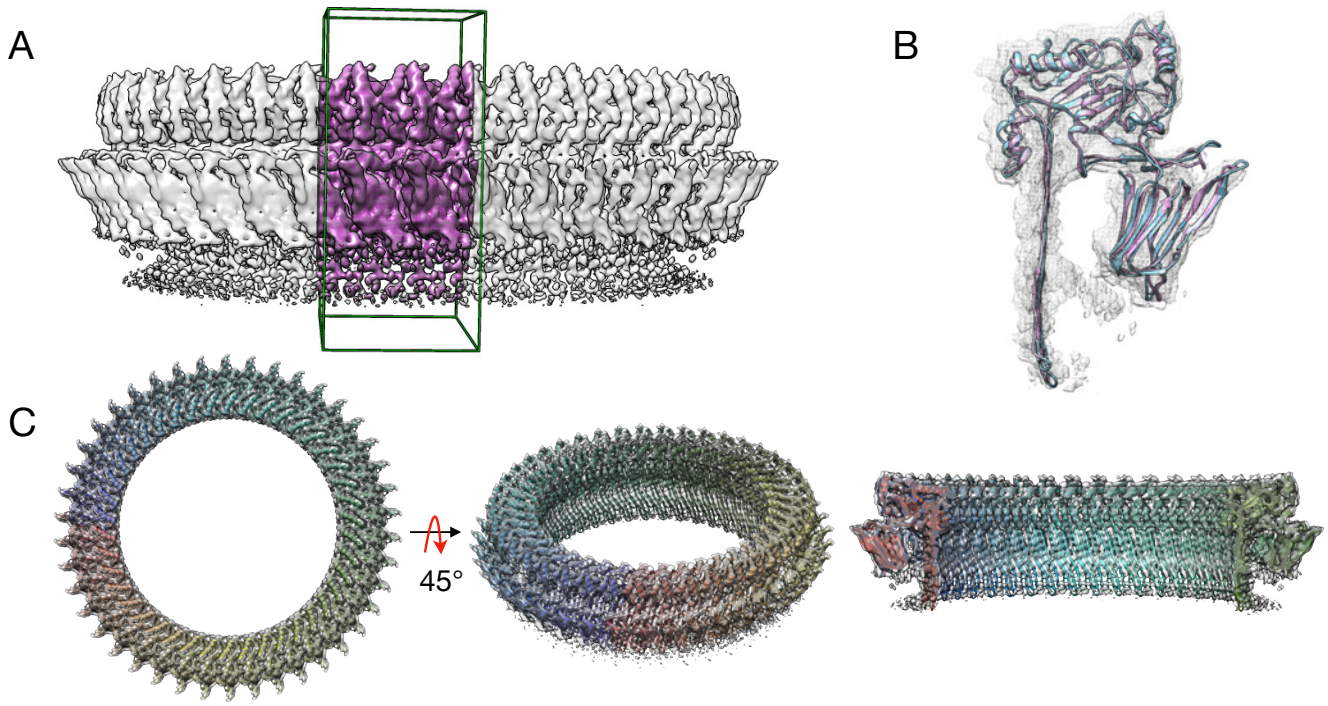

Fig. S20. Modeling pore conformation of PLY rings using molecular dynamics flexible fitting. (A) Cropped density (purple) from the complete ring density map of a PLY 42-mer ring (EMD-4118) (1) was used for fitting and refinement of the pore conformation. (B) All-atom model of PLY protomer fitted into the density map before (blue cartoon; CC=0.87) and after refinement by molecular dynamics flexible fitting (pink cartoon; CC=0.91; C_α RMSD=1.75 Å). (C) C_{42}-symmetrized protomers were simultaneously fitted into the density using a rigid-body fitting procedure and energy minimized to optimize lateral interactions forming the oligomeric ring structure of PLY (CC=0.92).

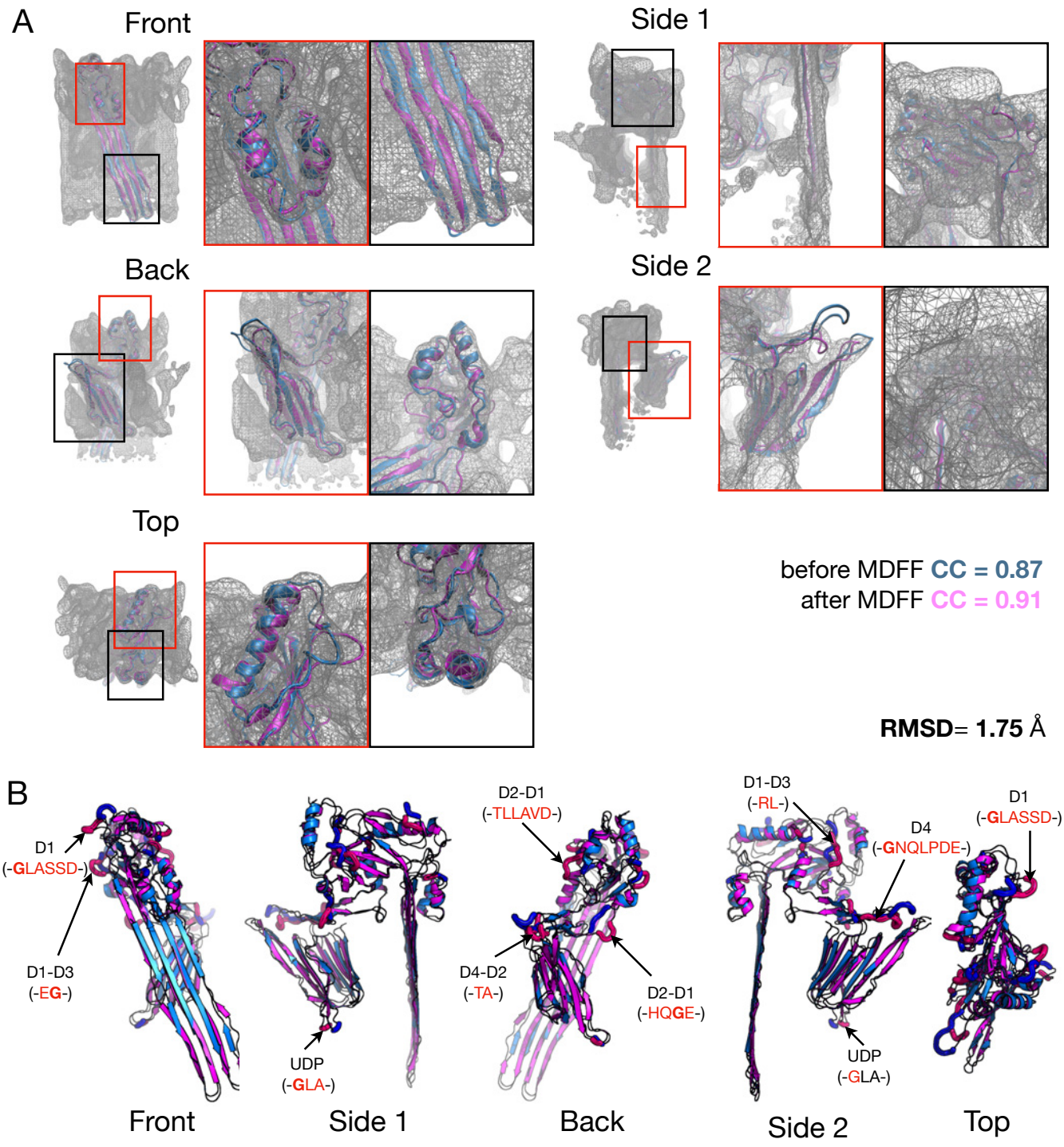

Fig. S21. Flexible fitting of PLY pore conformation. (A) Multiple views showing local fits (zoomed images, boxed) of PLY in pore conformation into the density map (grey mesh) before (blue cartoon; CC=0.87) and after refinement by molecular dynamics flexible fitting (pink cartoon; CC=0.91). (B) Comparison of the pore structure of PLY protomer before (blue) and after refinement (pink; C_α RMSD=1.75 Å). Conformational changes during MDFF are limited to flexible loops (highlighted tubes, labeled) connecting rigid regions of the PLY protomer. Gly residues (annotated sequence) in these loops allow conformational freedom, improving the local fit between the model and the map.

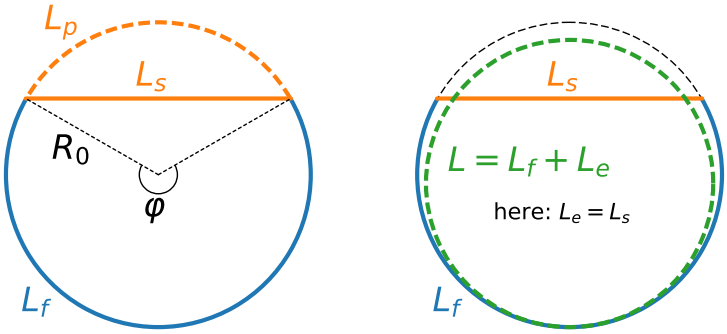

Fig. S22. Helfrich model for the PLY ring-enclosed membrane patches Left: Schematic of the circular membrane patch with circumference $2\pi R_0$. The length L_e of the open edge of the membrane facing the sector with PLY β-sheets inserted into the membrane (orange) varies between the arc length L_p of the sector and its secant L_s (i.e., $L_p \geq L_e \geq L_s$). An arc length L_f of the membrane is attached to the sector of the PLY ring in prepore conformation (blue). Right: The shape of the membrane patch in the partially inserted PLY ring is approximated as a spherical cap with uniform constant curvature to compute the bending energy. The spherical cap has a modified total circular edge, $L = L_f + L_e$ (green dashed line) with radius R such that $R \leq R_0$. The edge energy scales linearly with the exposed edge L_e due to membrane insertion of PLY-protomers in pore conformation. $L_e = L_p$ corresponds to a flat circular membrane disc with minimal or no curvature, whereas $L_e = L_s$ corresponds to the most curved cup-like shape of the spherical cap for a given fraction of inserted protomers.

Table S1. The four domains of PLY (39) along with other membrane interacting regions and the transforming helices (see Figure 1).

Region	Abbrev.	Residues
Domain 1	D1	1-13, 57-143, 201-243, 327-345
Domain 2	D2	14-56, 346-360
Domain 3	D3	144-157, 187-200, 244-255, 285-326
Domain 4	D4	361-471
Transforming helices	TH	158-186 256-284
Undecapeptide	UDP	427-437, Trp: 433,435,436
Loop 1	L1	458-461; esp. T459/L460

Table S2. Contact statistics for the atomistic and coarse-grained (CG) simulations of single docked PLY molecules. Out of all simulation frames with any kind of contact, we list the percentage of simulation frames in which contacts were formed between UDP or L1 residues on PLY and DOPC or cholesterol in the membrane. In the last two columns ("all"), we distinguish only between UDP and L1 contacts, but not between cholesterol and DOPC contacts.

Simulation	UDP+ cholesterol	UDP+ DOPC	L1+ cholesterol	L1+ DOPC	all UDP	all L1
atomistic	89.4	100.0	92.0	100.0	100.0	100.0
CG 0% cholesterol	0.0	96.1	0.0	84.2	96.1	84.2
CG 15% cholesterol	69.1	95.4	47.9	77.9	95.4	77.9
CG 30% cholesterol	89.9	97.3	55.8	70.1	97.3	70.1
CG 50% cholesterol	92.5	96.7	62.9	74.1	96.8	74.3
CG L460A	88.3	97.4	50.4	66.0	97.4	66.0
CG W433A+W435A+W436A	85.3	96.4	78.2	87.9	96.4	87.9
CG W433A	90.8	97.4	64.4	78.7	97.4	78.8

Table S3. Atomistic molecular dynamics simulations of PLY monomers and oligomers with starting structures in prepore (PLY) and pore conformation (PLY°) (see SI Fig. S4). Listed are the number of molecules for DOPC lipids, cholesterol, and solvent, the box width and height, and the simulation duration.

PLY starting structure	number protomers	number DOPC	number cholesterol	number solvent	width [nm]	height [nm]	time [ns]
PLY	1	943	0	160839	17.94(6)	18.99(14)	1060
PLY	1	749	321	159018	16.75(4)	21.41(11)	8010
PLY	1	385	165	56955	12.03(5)	16.43(14)	1050
PLY°	1	735	315	134884	16.73(7)	18.81(16)	1200
PLY°	1	735	315	139023	16.75(7)	19.20(15)	1200
PLY°	3	1127	483	196951	20.96(11)	17.92(18)	1100
PLY°	5	1113	477	210825	20.96(10)	19.11(18)	1100

Table S4. Coarse-grained simulations of PLY-membrane interactions. Coarse-grained MD simulations of PLY in prepore conformation were performed to study membrane binding and docking. Simulations of PLY (WT) were performed with varying degree of cholesterol concentrations. Mutant PLY structures with changes in undecapeptide and loop 1 residues were also modeled and simulated. 100 replicas were run for each system with different random seeds. Values for the box size and its standard deviation are averaged over all replicas. The number of molecules in the simulation systems is listed for DOPC lipids and cholesterol, together with the number of coarse-grained beads for water (which correspond to four atomistic molecules each).

System	cholesterol %	number DOPC	number cholesterol	number water	width [nm]	height [nm]	time [μs]
WT	0	1152	0	51005	19.86 $\pm$ 0.06	20.98 $\pm$ 0.14	2.0
WT	15	1148	202	51103	20.28 $\pm$ 0.06	20.39 $\pm$ 0.13	2.0
WT	30	1020	436	51275	19.82 $\pm$ 0.06	21.29 $\pm$ 0.13	2.0
WT	50	900	900	51460	20.15 $\pm$ 0.06	20.89 $\pm$ 0.13	2.0
L460A	30	1020	436	51268	19.82 $\pm$ 0.06	21.31 $\pm$ 0.13	2.0
W433A	30	1020	436	51283	19.82 $\pm$ 0.06	21.30 $\pm$ 0.13	2.0
W433A, W435A, W436A	30	1020	436	51276	19.82 $\pm$ 0.06	21.31 $\pm$ 0.13	2.0

Table S5. Coarse-grained simulations of fully formed PLY rings. Coarse-grained molecular dynamics simulations of single PLY_{42} ring in NPT ensembles were simulated with 8 intermediate configurations along the ring insertion pathway. The relative number of protomers in pore and prepore conformations were varied to make the intermediate configurations of PLY rings. The number of molecules in the simulation systems is listed for DOPC lipids and cholesterol, together with the number of coarse-grained beads for water (which correspond to four atomistic molecules each).

pore	pre-pore	number DOPC	number cholesterol	number water	width [nm]	height [nm]	time [μs]
0	42	12532	5370	988734	68.66 $\pm$ 0.26	32.35 $\pm$ 0.24	3.6
6	36	12194	5226	986639	66.98 $\pm$ 0.39	33.83 $\pm$ 0.40	3.6
11	31	12169	5214	987992	67.21 $\pm$ 0.37	33.62 $\pm$ 0.37	3.6
16	26	12148	5205	985958	67.32 $\pm$ 0.36	33.45 $\pm$ 0.35	3.6
21	21	12120	5193	985687	67.98 $\pm$ 0.45	32.79 $\pm$ 0.44	3.6
26	16	12088	5180	985164	67.30 $\pm$ 0.34	33.42 $\pm$ 0.33	3.6
31	11	12071	5172	984932	67.46 $\pm$ 0.31	33.25 $\pm$ 0.30	3.6
36	6	12047	5163	982264	66.58 $\pm$ 0.44	34.05 $\pm$ 0.45	3.6
42	0	12025	5153	985391	67.14 $\pm$ 0.32	33.56 $\pm$ 0.32	3.6

Table S6. Coarse-grained simulations of two PLY rings. Two identical inverted PLY$_{42}$ rings were embedded in cholesterol-rich DOPC bilayers and simulated in an NP_zT ensemble to permit free lipid-flow in and out of the rings. The relative number of protomers in pore and prepore conformation was varied to mimic various intermediate ring configurations along an insertion pathway. The number of molecules in the simulation systems is listed for DOPC lipids and cholesterol, and the number of coarse-grained beads (each corresponding to four atomistic molecules) for water.

pore	pre-pore	number DOPC	number cholesterol	number water	L_x [nm]	L_y [nm]	L_z [nm]	time [μs]
0	42	24460	10482	1989966	70	140	31.21 $\pm$ 0.01	3.00
6	36	24388	10452	1973344	70	140	30.97 $\pm$ 0.01	3.00
11	31	24338	10428	1975940	70	140	31.00 $\pm$ 0.01	3.00
16	26	24296	10410	1971988	70	140	30.94 $\pm$ 0.01	3.00
21	21	24240	10386	1971168	70	140	30.91 $\pm$ 0.01	3.00
26	16	24176	10360	1970418	70	140	30.89 $\pm$ 0.01	3.00
31	11	24142	10344	1969724	70	140	30.88 $\pm$ 0.01	3.00
36	6	24094	10326	1964450	70	140	30.80 $\pm$ 0.01	3.00
42	0	24050	10306	1970678	70	140	30.88 $\pm$ 0.01	3.00

Supplementary Movie files (attached).

Movie S1. Atomistic simulation of PLY pentamer model.

Movie S2. Coarse-grained simulation of a PLY ring with all protomers in prepore conformation (0/42).

Movie S3. Coarse-grained simulation of a PLY ring with all protomers in pore conformation (42/42).

Movie S4. Coarse-grained simulation of a PLY ring with 50% of protomers in prepore conformation and 50% of protomers in pore conformation (21/42).

References

1. van Pee K, et al. (2017) CryoEM structures of membrane pore and prepore complex reveal cytolytic mechanism of pneumolysin. *eLife* 6:1–22.
2. Pettersen EF, et al. (2004) UCSF Chimera - A visualization system for exploratory research and analysis. *J Comput Chem* 25(13):1605–1612.
3. Trabuco LG, Villa E, Schreiner E, Harrison CB, Schulten K (2009) Molecular dynamics flexible fitting: A practical guide to combine cryo-electron microscopy and X-ray crystallography. *Methods* 49(2):174–180.
4. Humphrey W, Dalke A, Schulten K (1996) VMD: Visual molecular dynamics. *J Mol Graph* 14(1):33–38.
5. Huang J, et al. (2016) CHARMM36m: An improved force field for folded and intrinsically disordered proteins. *Nat Methods* 14(1):71–73.
6. Phillips JC, et al. (2005) Scalable molecular dynamics with NAMD. *J Comput Chem* 26:1781–1802.
7. Schneidman-Duhovny D, Inbar Y, Nussinov R, Wolfson HJ (2005) Geometry-based flexible and symmetric protein docking. *Proteins* 60(2):224–231.
8. Schneidman-Duhovny D, Inbar Y, Nussinov R, Wolfson HJ (2005) PatchDock and SymmDock: Servers for rigid and symmetric docking. *Nucleic Acids Res* 33(SUPPL. 2):363–367.
9. Lasker K, Sali A, Wolfson HJ (2010) Determining macromolecular assembly structures by molecular docking and fitting into an electron density map. *Proteins* 78(15):3205–3211.
10. Marshall JE, et al. (2015) The crystal structure of pneumolysin at 2.0 Å resolution reveals the molecular packing of the pre-pore complex. *Sci Rep* 5(July):13293.
11. Lomize AL, Pogozheva ID, Lomize MA, Mosberg HI (2006) Positioning of proteins in membranes: A computational approach. *Protein Sci* 15(6):1318–1333.
12. Lomize AL, Pogozheva ID, Mosberg HI (2011) Anisotropic solvent model of the lipid bilayer. 2. Energetics of insertion of small molecules, peptides, and proteins in membranes. *J Chem Inf Model* 51(4):930–946.
13. Lomize MA, Pogozheva ID, Joo H, Mosberg HI, Lomize AL (2012) OPM database and PPM web server: Resources for positioning of proteins in membranes. *Nucleic Acids Res* 40(D1).
14. Jo S, Kim T, Iyer VG, Im W (2008) CHARMM-GUI: A web-based graphical user interface for CHARMM. *J Comput Chem* 29(11):1859–1865.
15. Jo S, Lim JB, Klauda JB, Im W (2009) CHARMM-GUI membrane builder for mixed bilayers and its application to yeast membranes. *Biophys J* 97(1):50–58.
16. Wu EL, et al. (2014) CHARMM-GUI membrane builder toward realistic biological membrane simulations. *J Comput Chem* 35(27):1997–2004.
17. Lee J, et al. (2016) CHARMM-GUI Input Generator for NAMD, GROMACS, AMBER, OpenMM, and CHARMM/OpenMM Simulations Using the CHARMM36 Additive Force Field. *J Chem Theory Comput* 12(1):405–413.
18. Pandit KR, Klauda JB (2012) Membrane models of E. coli containing cyclic moieties in the aliphatic lipid chain. *Biochim Biophys Acta, Biomembr* 1818(5):1205–1210.
19. Klauda JB, et al. (2010) Update of the CHARMM All-Atom Additive Force Field for Lipids: Validation on Six Lipid Types. *J Phys Chem B* 114(23):7830–7843.
20. Abraham MJ, et al. (2015) Gromacs: High performance molecular simulations through multi-level parallelism from laptops to supercomputers. *SoftwareX* 1-2:19–25.
21. Jorgensen WL, Chandrasekhar J, Madura JD, Impey RW, Klein ML (1983) Comparison of simple potential functions for simulating liquid water. *J Chem Phys* 79(2):926–935.
22. Nosé S (1984) A unified formulation of the constant temperature molecular dynamics methods. *J Chem Phys* 81(1):511–519.
23. Hoover WG (1985) Canonical dynamics: Equilibrium phase-space distributions. *Phys Rev A* 31(3):1695–1697.
24. Parrinello M, Rahman A (1981) Polymorphic transitions in single crystals: A new molecular dynamics method. *J Appl Phys* 52(12):7182–7190.
25. Hess B, Bekker H, Berendsen HJC, Fraaije J (1997) LINCS: A linear constant solver for molecular simulations. *J Comput Chem* 18(12):1463–1472.
26. Berendsen HJC, Postma JPM, van Gunsteren WF, DiNola A, Haak JR (1984) Molecular dynamics with coupling to an external bath. *J Chem Phys* 81(8):3684–3690.

27. Bussi G, Donadio D, Parrinello M (2007) Canonical sampling through velocity rescaling. *J Chem Phys* 126(1):014101.
28. Chinea G, Padron G, Hooft RWW, Sander C, Vriend G (1995) The use of position-specific rotamers in model building by homology. *Proteins* 23(3):415–421.
29. Wassenaar TA, Ingólfsson HI, Böckmann RA, Tieleman DP, Marrink SJ (2015) Computational lipidomics with insane: A versatile tool for generating custom membranes for molecular simulations. *J Chem Theory Comput* 11(5):2144–2155.
30. Phillips R (2017) Membranes by the Numbers. *ArXiv e-prints* p. 1703.02066. https://arxiv.org/abs/1703.02066.
31. Tilley SJ, Orlova EV, Gilbert RJC, Andrew PW, Saibil HR (2005) Structural basis of pore formation by the bacterial toxin pneumolysin. *Cell* 121(2):247–256.
32. Helfrich W (1973) Elastic properties of lipid bilayers: Theory and possible experiments. *Z Naturforsch C* 28(11):693.
33. Capovilla R, Guven J, Santiago JA (2002) Lipid membranes with an edge. *Phys Rev E* 66(2):1–7.
34. Tu ZC, Ou-Yang ZC (2003) Lipid membranes with free edges. *Phys Rev E* 68(6):1–7.
35. Van Pee K, Mulvihill E, Müller DJ, Yildiz Ö (2016) Unraveling the pore-forming steps of pneumolysin from Streptococcus pneumoniae. *Nano Lett* 16(12):7915–7924.
36. Sonnen AF, Plitzko JM, Gilbert RJ (2014) Incomplete pneumolysin oligomers form membrane pores. *Open Biol* 4:140044.
37. Song J, Waugh RE (1993) Bending rigidity of SOPC membranes containing cholesterol. *Biophys J* 64(6):1967–1970.
38. Jiang FY, Bouret Y, Kindt JT (2004) Molecular dynamics simulations of the lipid bilayer edge. *Biophys J* 87(1):182–192.
39. Köster S, et al. (2014) Crystal structure of listeriolysin O reveals molecular details of oligomerization and pore formation. *Nat Commun* 5:3690.